City, University of London Institutional Repository

This is the accepted version of the paper.

This version of the publication may differ from the final published version.

Improving Purge Air Cooling Effectiveness by Engineered End-Wall Surface Structures – Part I: Duct Flow

Xin Miao
e-mail: Xin.Miao@city.ac.uk

Qiang Zhang
e-mail: Qiang.Zhang.1@city.ac.uk

Chris Atkin
e-mail: Chris.Atkin.1@city.ac.uk

Zhengzhong Sun
e-mail: Zhengzhong.Sun@city.ac.uk

Department of Mechanical Engineering & Aeronautics
City University London
Northampton Square, London, EC1V 0HB, United Kingdom

Y S Li
e-mail: yansheng.li@siemens.com
Siemens Industrial Turbomachinery Limited
Lincoln LN5 7FD, UK

ABSTRACT

Motivated by the recent advances in Additive Manufacturing (AM), this study investigated a new turbine end-wall aerothermal management method by engineered surface structures. The feasibility of enhancing purge air cooling effectiveness through a series of small-scale ribs added onto the turbine end-wall was explored experimentally and numerically in this two-part paper. Part I presents the fundamental working mechanism and cooling performance in a 90-degree turning duct (Part I), and Part II of this paper validates the concept in a more realistic turbine cascade case.

In Part I, the turning duct is employed as a simplified model for the turbine passage without introducing the horseshoe vortex. End-wall heat transfer and temperature were measured by the infrared thermography. CFD simulation was also performed using ANSYS FLUENT to compliment the experimental findings. With the added end-wall rib structures, purge air flow was observed to be more attached to the end-wall and cover a larger wall surface area. Both experimental and numerical results reveal a consistent trend on improved film cooling effectiveness. The practical design optimization strategy is also discussed in this paper.

INTRODUCTION

Efficient cooling techniques have been essential for modern gas turbines to safely operate at the extremely high temperature environment [1]. In the turbine stage, the high pressure hot gas may enter the cavity between the stator and rotor, which causes over-heating, thermal fatigue, and dilatation of the discs. A stream of cold air from the compressor is introduced to eject through the rim seal to prevent hot gas ingestion. Recently, purge air cooling also becomes one of the widely used methods to effectively protect the turbine end-wall.

Some of early purge air studies focused on the simplified cavity configurations and the heat transfer problems inside the cavities. Bunker et al. [2-3] measured the heat transfer coefficients distribution in three basic disk-cavity geometries. Wilson et al. [4] performed Direct Navier-Stokes (DNS) calculation to predict the highly unsteady flow within a rotating cavity, simulating the realistic working condition. The aerodynamic effect due to interaction between the mainstream and purge air flow also received many attentions. McLean et al. [5-6] studied three different purge air injection configurations, and found that cooling flows by root injection can reduce the flow over-turning and under-turning. Even with a small injection rate, purge air can generate a high aerodynamic loss.

Girgis et al. [7] tested a transonic turbine with various secondary air injection conditions. They found that cavity flows with a large tangential component allow an improvement of 10.3% efficiency compared to the case of flow injected radially. Reid et al. [8] reported that the turbine efficiency decreases with increasing purge flow rate, but this penalty is reduced by swirling the purge flow.

A substantial amount of efforts have been made to investigate turbine blade end-wall cooling with the purge air. The study of Roy et al. [9] showed that the heat transfer near the leading edge region is reduced due to the upstream purge air injection and a higher purge air mass ratio is also beneficial in weakening the passage vortex. Similar results were also observed by Burd et al. [10] and Oke et al. [11]. Dénos and Paniagua [12] studied the purge air effect in a high-pressure transonic turbine stage. They found the purge air effectively reduces the heat flux around the rotor leading edge. Wright et al. [13-14] measured film cooling effectiveness of different purge slot geometries by pressure sensitive paint technique. Their results show that the large purge air ratio could not only offer cooling protection to the rear of the blade passage, but also result in a large aerodynamic penalty. In addition, combining both upstream purge air and downstream film holes can efficiently increase film cooling effectiveness. Popovic and Hodson [15] investigated a highly-loaded rotor blade with purge air injection, and observed that the purge air mainly concentrates around the blade suction surface, resulting in a higher heat transfer coefficient, however, the overall heat load is not reduced.

The latest advances in manufacturing techniques, especially Additive Manufacturing (AM), offer an increased design space and flexibility to turbine

aerothermal management. Engineered surface features now could be efficiently fabricated and applied, providing a good physical understanding on the flow-structure interaction. Previous study of Miao et al. [16-17] reported that adding small-scale ribs with streamline shapes on the turbine end-wall could be very effective in reducing the passage secondary flow. The concept was verified both in a 90-degree turning duct and a linear cascade condition. The near wall low momentum fluids can be aligned by the engineered surface "guides" and the over-turning can be alleviated effectively.

This novel flow control technique could also be used for purge air cooling enhancement: engineered small-scale surface ribs can also be envisaged as the devices for controlling and aligning the purge air cooling flow. This two-part paper explores the feasibility of this new concept through closely coupled experimental and numerical studies. Part I of this paper presents the investigation of purge air cooling on the end-wall of a simplified duct flow. Studying this simplified flow model is useful in obtaining fundamental physical understanding on the working mechanism of this flow control concept without considering the complex horseshoe vortex developed in the turbine system. Part II of this paper fully validates the concept in a turbine cascade case. Transient thermal measurement technology was employed to obtain adiabatic wall temperature and the heat transfer coefficient. A RANS solver by commercial CFD code (ANSYS FLUENT) was used for the numerical simulation which provides further insights into the detailed flow physics.

EXPERIMENTAL APPARATUS AND PROCEDURES

Low-Speed Wind Tunnel and Test Section

A low-speed wind tunnel facility was used in the present study. The flow is driven by a 25 kW air blower. A settling chamber with mesh screens is located upstream of the contraction section. This wind tunnel was also equipped with a heating mesh powered by a 100 kW DC power supply to generate a step increase in temperature in the flow. The heating mesh was made of stainless steel with a sieve mesh number of 200. The outlet of the contraction is 100 mm in height (H) and 50 mm in width (D), and delivers a velocity of 20 m/s. Note that the duct height H was chosen to be 2D to avoid the interaction between the induced passage vortex and the top wall. The Reynolds number based on the duct width D is 69,000.

A schematic of the test section is shown in Fig.1. The non-dimensional radius ratio of the duct was kept the same as that in Camci et al. [18]. The inner and outer radius ratios (r_i/D and r_o/D) are 1.8 and 2.8, respectively. The turning duct was equipped with straight inlet and outlet sections, whose lengths are 2.5D. The bottom end-wall on the duct channel was designed with inter-changeable blocks. Two types of end-wall blocks were employed: one smooth wall and one with seven small-scale ribs. The end-wall block with ribs were manufactured through 3D printing and the ribs cover the angular range from 0° to 45°, namely the first half of the turning duct. The rib array geometry is summarized in Table 1.

Transient Infrared thermal measurement was conducted on the end-wall surface. A zinc selenide window was fitted into the duct top wall and an infrared camera was installed perpendicularly with respect to the IR window. The distance from IR camera to the window was adjusted to ensure the field of view covers an angular region between 45 ° to 90 °, namely the latter half of the turning duct, as shown in Fig.1.

Two fast-response thermocouples were placed in the inlet section and purge cavity respectively to monitor their temperatures. The thermocouple has a wire diameter of 76 μm and response time of less than 80 ms. The temperature was recorded by a National Instrument data acquisition system.

Figure 2 presents the inlet boundary layer profile measured by using a boundary layer probe with a flat tip. A typical turbulent boundary layer characteristic can be observed. The Inlet boundary layer thickness and shape factor are 6mm and 1.3 respectively. The turbulence level of the flow is about 1%. The stagnation and static pressures of the test section inlet were measured by a pitot tube.

A vortex tube was used to generate the cold air sent through the purge cavity. The vortex tube was connected to a compressed air supply. The cold end of the tube connects to a stabilizing cavity with a steady temperature of 278 K throughout the transient tests. An inclined slot on top of the cavity injects the cold air into the turning duct, thus forming the purge air flow. The slot outlet has an inclination angle of 30-degree with respect to the wall. The slot spans along the entire duct width and has a width of 0.06 D. The volumetric flow rate of the purge air was measured by using a digital flow meter. The ratio between the purge air velocity and the freestream is 0.86. The choice of the slot

dimensions and flow conditions was based on an early experiment work by Wright et al. [14].

In-Situ Calibration of Infrared Camera

In-situ calibration of the IR camera similar to previous research by Schulz [19], O'Dowd et al [20], and Zhang et al. [21] was conducted in the present study. A fast-response thermocouple was imbedded in the middle of the end-wall to record temperature variation. Its location is a good representative of the nearby region which should share similar emissivity, view factor, IR window transmissivity, etc. Figure 3 presents a linear calibration relationship between the 16-bit grayscale values from the infrared camera and the temperature readings obtained by the thermocouple during a transient run. The temperature to grayscale resolution of the IR camera is 0.002 ℃ per grayscale value. The systematic error should mainly come from the thermocouple (1K) reading.

Transient Thermal Measurement and Data Processing

Figure 4a presents the time histories of the cold purge air, end-wall and inlet temperatures during a typical transient experiment. After a step heating by the heater mesh, the mainstream temperature (red color) and the temperate of cold purge air (blue color) were maintained at a relatively constant value for a short period of time.

For an established flow field near the end-wall surface, the heat transfer coefficient can be defined as,

$$q'' = h(T_{ad} - T_w) \tag{1}$$

where q'' is the heat flux, T_{ad} is adiabatic wall temperature, T_w is end-wall temperature.

For the solid side, it is reasonable to assume one dimensional semi-infinite conduction due to the low conductivity material employed for the end-wall surface. The local heat flux can be calculated based on the transient wall temperature history. In this study, a well-established Impulse Response Method, developed by Oldfield [24] and further implemented by a series of research by O'Dowd et al. [20], Zhang et al. [21-23], and Ma et al [24], was employed. This method uses discrete deconvolution and a pair of nonsingular analytical solutions to the convective heat transfer equation to derive a digital filter impulse response, then the heat flux can be determined from temperature traces based on the convolution integral. The measured thermal product $\sqrt{\rho C \kappa}$ of the end-wall material is 564 $\sqrt{s}$/m²K (previously reported by Ma et al [25]).

Figure 4b shows the time history of local heat flux (calculated) and wall temperature (measured) for a sample location on the end-wall during one transient measurement. Both heat flux and temperature values were non-dimensionalized. All the data points in Fig. 4b follow a linear trend, which indicates and proves the validity of the convection equation (1) and satisfactory accuracy of the transient experiments. Both heat transfer coefficient and adiabatic wall temperature can be obtained from linear regression: the slope of the regression line is the Nusselt number and the *x*-axis interception is the adiabatic wall temperature.

Uncertainty Analysis

A jitter analysis described by Moffat [26] was used to determine the overall uncertainty in the experimental study. The sources of experimental uncertainty include measured wall temperature, material properties, the calibration of the IR camera, mainstream and coolant temperature variations and measurement, etc. For transient thermal measurement and the Impulse method employed in the present work, the linear regression error also needs to be considered. A coefficient of determination R^2, defined by Devore [26], is calculated to assess the linear regression performance. Figure 5 presents a detailed distribution of R^2 in the measurement area for the smooth end-wall case. For the majority of the measurement region, R^2 is well above 0.9.

The 95% confidence level was used to estimate the uncertainty in the transient thermal measurement. Four repeated transient tests were taken for each type of end-wall surface. Figure 5b shows the contour of relative uncertainty in adiabatic wall temperature. The relative uncertainty in T_{ad} is below 0.5% for most of the test surface.

In the present experimental study, the element systematic error sources mainly come from the wall temperature measurement and the determination of end-wall material property (also reported previously by O'Dowd et at. [20]).

Table 2 presents a summary of uncertainty values for various measurement properties.

CFD METHOD and Validation

The flow in the present turning duct was simulated by using the commercial CFD software ANSYS FLUENT. The computational domain is shown in Fig. 6. The geometry and the duct inlet flow condition were set the same as the experiments. The measured inlet velocity profile shown in Fig. 2 was implemented by a User Defined Function (UDF) code programmed in C language. An ambient pressure was set as the duct outlet boundary condition. Isothermal boundary conditions were set on the end-walls. The heat transfer coefficient and adiabatic wall temperature were calculated from two cases with different end-wall temperature values (290 K and 300 K).

Structured grids, generated through the commercial software Pointwise, were employed for the entire flow domain. Figure 5 presents an enlarged view of the hexahedra mesh around the purge air slot and wall ribs. The first grid point immediately above the wall has y^+ value of less than 1.

The flow solver uses the finite volume method to solve the Steady three-dimensional Reynolds-Averaged Navier-Stokes (RANS) equations. The k-ω shear stress transport (SST) turbulence model was chosen for all the numerical studies. The simulation was carried out in the double-precision mode to improve the level of convergence.

The simulation strategy is validated through the comparison with the experimental data from Camci and Rizzo [18]. In their study, a similar 90-degree turning duct with a single fence on the end-wall was used. Note that this case study is only for validation purpose, and the aspect ratio of the duct is different from all the other cases with purge air injection.

Grid independence was first checked in this single fence case through three grids with different density, namely 2 million, 5 million and 8 million nodes. Figure 7 compares the spanwise-averaged total loss coefficient C_p at the exit of turning passage (90-degree plane). The grid of 5 million nodes is chosen for all other simulation cases since the maximum difference between results from the grids of 5 million and 8 million nodes is less than 5%.

Figure 8 presents the coefficient of total pressure loss at the exit plane. An overall agreement can be observed. In the plane without rib fence, the region with larger total pressure loss is associated with the passage vortex pair, and it features a symmetric mushroom-type due to the interaction of fluids between top and bottom walls. Because of the presence of rib fence and the resulted smaller vortex, the total pressure loss is alleviated in the lower half of the "mushroom". As such, the present CFD methodology is able to qualitatively demonstrate the detailed secondary flow structure in a curved channel flow, with acceptable quantitative accuracy. Further comparison with thermal measurement will be discussed in later sections.

RESULTS AND DISCUSSIONS

In this section, the purge air flow structure and its interaction with the passage secondary flow are firstly shown based on CFD analysis. The cooling enhancement mechanism with the ribbed surface is then discussed, after which experimental data of cooling effectiveness, heat transfer coefficient and Net Heat Flux Reduction (NHFR) are presented and the CFD results are validated.

Purge Air Flow Structure

The working mechanism of purge air cooling is quite similar to conventional film cooling technique. A thin layer of low temperature air is expected to effectively cover the end-wall surface. To visualize the cold purge air coverage area, Figure 9 shows an iso-temperature surface θ, defined as,

$$\theta = \frac{T-T_c}{T_\infty-T_c} = 0.6 \tag{2}$$

where T_c is the cold purge air temperature, T_∞ is mainstream temperature and T is the local temperature. The parameter θ also represents the purge air concentration (a lower θ value indicates a colder local fluid temperature).

For the smooth end-wall case, driven by radial pressure gradient, the iso-temperature surface associated with cold purge air quickly sweeps towards the duct inner side. Figure 9b shows that the ribbed surface effectively extends the iso-temperature further downstream from about 45° to about 60°, after which the three-dimensional vortical motion occurs.

Figure 10 shows the non-dimensional fluid temperature θ distribution at three angular cross sections along the duct passage. The cross sections are located at 30°, 45° and 60° of the turning duct. In the duct with smooth end-wall surface, the low temperature air gradually moves from the outer wall to inner wall as the fluid travels along the passage. At the 60° plane, most of the cold air lifts off away from the end-wall and the passage vortex contains a majority of the purge air. In contrast, for the ribbed surface, most purge air can stay near the end-wall and fully occupies the rib channels at both 30° and 45° cross sections, and this is even more apparent at the 60° section.

Compared with the smooth case, the near end-wall fluid temperature with ribs is much lower.

The secondary flow in the turning duct is associated with the streamwise component of vorticity. Three typical radial cross-sectional planes at 30°, 45° and 60° were extracted to reveal the evolution of the secondary flow, as shown in Fig. 11. The streamwise vorticity is defined as the tangential component in a cylindrical coordinate system, and it can be calculated by,

$$\Omega_s = \Omega_x sin\beta + \Omega_y cos\beta \qquad (3)$$

Where β is labeled in Fig. 1. In Fig. 11, the streamwise vorticity is further nondimensionalized by D/V_∞. The negative vorticity (red in color), is associated with the secondary flow vortex, while the positive vorticity (blue in color) represents the vortex with an opposite direction of rotation to the secondary flow vortex. Figure 11a shows that, in the duct with smooth end-wall, concentration of negative vorticity gradually builds up at the lower inner-corner within the selected angular range, suggesting the growth of the secondary flow vortex. In Fig. 11b, the ribs on the end-wall surface modify the vorticity distribution throughout the angular range. Apparently, the intensity of negative vorticity associated with the secondary flow vortex is reduced. In the smooth surface duct, the secondary flow accumulates in the inner-end-wall corner and gradually extends along the inner vertical wall; however, the presence of the ribs effectively eliminates this accumulation of secondary flow. The ribs also introduce vortices with an opposite sign, which have been revealed as vortices of smaller scale than the secondary

flow vortex. Since the ribs only extend from 0° to 45° in the present design, the array of positive vorticity associated with these ribs disappears in the cross section at 60°.

Next, the overall aerodynamic performance is evaluated for cases with and without end-wall ribs. In order to account for all the contributions due to viscous effects and heat transfer between the mainstream and purge flow, the aerodynamics loss coefficient is defined as

$$\zeta = 1 - \frac{\left(\dot{m}_c \cdot C_{p,c} \cdot T_{0,c} + \dot{m}_{in} \cdot C_{p,in} \cdot T_{0,in}\right)\left(1 - \left(\frac{P}{P_0}\right)^{\left(\frac{\gamma-1}{\gamma}\right)}\right)}{\dot{m}_{in} \cdot C_{p,in} \cdot T_{0,in}\left(1 - \left(\frac{P_{mid}}{P_{0,in}}\right)^{\left(\frac{\gamma-1}{\gamma}\right)}_{in}\right) + \dot{m}_c \cdot C_{p,c} \cdot T_{0,c}\left(1 - \left(\frac{P_{mid}}{P_{0,c}}\right)^{\left(\frac{\gamma-1}{\gamma}\right)}_{c}\right)} \quad (4)$$

Figure 12 shows the distribution of aerodynamics loss coefficient at the 90-degree plane in the smooth and ribbed cases. It can be observed that the loss core of the passage vortex is close the end-wall with the addition of ribs. In the corner region between inner wall and end-wall the loss is increased slightly. The mass-averaged loss coefficient between smooth and ribbed cases is less than 2%. The additional aerodynamic penalty introduced by the small ribs is negligible.

Cooling Effectiveness and Net Heat Flux Reduction (NHFR)

Film cooling effectiveness measured for both types of end-walls is presented and further compared with CFD analysis in this section. The calculation of film cooling effectiveness η follows the relation below

$$\eta = \frac{T_\infty - T_{ad}}{T_\infty - T_c} \quad (5)$$

where T_c is the cold purge air temperature, T_∞ is the mainstream temperature and T_{ad} is the adiabatic wall temperature.

Figure 13 presents the contours of η obtained in the experiments for both end-walls. The region of higher η, namely η>0.5, can be clearly observed in Fig. 13a. At the angular position of 45°, the high film cooling efficiency only covers about half of the duct width, while the highest η is close to the inner side wall. The region of high η quickly shrinks in size further downstream and it fully disappears after 70°. The rapid decay of cooling effectiveness is caused by the sweeping effect of the secondary flow vortex, which carries the cold purge air flow away from the end-wall towards the inner curved wall through its vortical motion. In contrast, the ribbed surface has improved the cooling performance significantly, as shown in Fig. 13b. The region of η>0.5 covers the entire duct width at angular position of 45°, whilst the high η region extends further downstream till 80° near the inner wall. The total area with good cooling air coverage over the ribbed surface is about twice of that over the smooth surface. Some very high η regions with η>0.7 can still be observed, and they are aligned with the grooves formed between adjacent ribs. This discrete distribution of high cooling effectiveness region is due to the near wall small scale vortex array generated by the ribs (previously shown in Fig. 11). It seems that these small vortices are very efficient in maintaining the purge air flow close to the end-wall surface. On the other hand, Fig. 13b also shows a few discrete blue stripes aligned with the rib locations, which indicate a poor coolant coverage over the top surfaces of the ribs upstream. This issue will be further discussed in later section.

Figure 14 shows film cooling effectiveness calculated by numerical simulation. The qualitative trend is consistent. The simulation has a reasonably good agreement with the experimental data in terms of the overall cooling effectiveness distribution and the enhancement by the ribs is also quite similar in terms of the increased coverage area. Very high cooling performance inside the rib grooves can be observed by the simulation. both experiment and CFD results confirm that the ribbed surface enables cooling enhancement by maintaining the cold purge air attached to the end-wall to a much larger extent. Quantitively, the CFD data are less diffused than the measurement results. Nearly no cooling flow can be observed from some of the grooves near the outer wall, while there is more cooling coverage near the inner wall region. Such discrepancy is a common performance from a standard RANS solver. The interaction between secondary flow and cooling fluid needs to be better resolved by CFD solvers with high-fidelity.

Figure 15 further illustrate the laterally-averaged film cooling effectiveness along the duct passage by comparing results from the smooth (black color) and ribbed surfaces (red color). The CFD result is shown as dash lines, while the experimental data is presented as solid lines. After the 20° location, a rapid decline of the $\bar{\eta}$ value can be observed because the passage vortex sweeps the purge air from outer wall to inner wall. For ribbed surface, the $\bar{\eta}$ starts from about 0.85 since the purge air is not able to fully cover the tip surface of the rib structure (this can also be observed in Fig. 14b, and will be further discussed later). Due to the blockage effect of rib structure, the early overturning of the purge air is largely reduced, and more cooling air can stay near the end-wall. Therefore, comparing with the results from the smooth case the value for the ribbed

surface decreases more gradually. The experimental data have very good agreement with CFD results both qualitatively and quantitatively in the region where test data is available.

Figure 16 shows a quantitative comparison of the local film cooling effectiveness variation along the radial direction at the angular position of 50°. Solid lines and dash lines are used to represent the experimental data and CFD result, respectively. Consistent Figs. 13 and 14, a significant increase of film cooling effectiveness can be observed at r/R>0.5 due to the guidance effect of ribs. The underprediction of coolant coverage near the outer wall region from CFD can also be consistently found for both smooth and ribbed walls.

The contours of heat transfer coefficient on the smooth and ribbed surfaces are shown in Fig. 17. Some stripes with high values of heat transfer coefficient can be observed near the end of the ribs, where the flow is dominant by small vortices developed earlier in the rib grooves. But there is a significant reduction of heat transfer coefficient for the majority of the after-rib region due to the relatively slower convection speed of the near wall coolant. Figure 18 presents the heat transfer coefficient distribution obtained by CFD simulation. There is a consistent agreement with the experimental data at the 45° to 90° region. For the smooth surface case, a low the heat transfer coefficient region from 20° to 45° can be observed. This is related to the lift-off of the passage vortex from the end-wall. With the addition of ribs, the heat transfer coefficient is largely increased within the grooves due to small vorticies previously shown in Fig. 11.

To assess the overall cooling performance, the net reduction in heat flux relative to an uncooled smooth end-wall case is discussed next. Net Heat Flux Reduction (NHFR),

previously defined by Sen et al. [28], is the fractional decrease in heat flux due to film cooling,

$$NHFR = 1 - \frac{q_f''}{q_0''} \tag{6}$$

In the present study, q_f'' represents the heat flux for ribbed surface with film cooling, and q_0'' represents the heat flux for smooth surface without film cooling.

For end-wall region without ribs, the NHFR can be further written as:

$$\Delta q_r = 1 - \frac{h_f}{h_0}(1 - \eta\varphi) \tag{7}$$

The non-dimensional metal temperature φ is defined as:

$$\varphi = \frac{T_\infty - T_c}{T_r - T_b} \tag{8}$$

where T_∞ is the mainstream temperature, T_c is the coolant total temperature, T_b is the blade metal temperature, T_r is the recovery temperature. A value of 1.6 is used for typical engine conditions (Sen et al. [28]).

The NHFR distributions on the smooth and ribbed surfaces in the experiments are shown in Fig. 19. The blue color represents the region with low heat flux reduction, while the red color corresponds to the region benefiting from purge air cooling. CFD results in Figure 20 shows a similar pattern as the experimental data. With the addition of rib structure, more area of the end-wall region can benefit from purge air cooling.

Practical Considerations and Design Optimization Strategy

For practical application in turbine system, the ribbed surface has to be fully protected by the coolant without being exposed to the hot gas. Even with a significant

improvement in NHFR, the rib design has to be carefully optimized to achieve a reasonable level of cooling effectiveness near the rib structures for their long-term survival.

As pointed out in the previous discussions, there is a poor coolant coverage over the rib top surface near the duct entry region. The non-dimensional temperature θ distribution near entry region is shown in Fig.21a for the previous ribbed end-wall design. The purge air injected through the slot blocks the cooling fluid and it cannot reach the top surface the rib. Apparently the rib height selected needs to be further optimized.

An improved cooling performance is achieved from another optimized CFD case with 40% reduction of overall rib height, as illustrated in Fig. 21b and Fig. 22. The film cooling effectiveness near the upstream region is significantly enhanced by adding ribs with an optimal height.

Another region which deserves further attention is the ribs close to outer wall. The discrete blue stripes shown from the experimental data in Fig. 13b, as well as the low η region near the duct outer wall in Fig. 22, indicate the ribs could be vulnerable for hot gas. Figure 23 presents fluid streamlines colored by temperature which illustrate the development of purge air flow within the grooves of the ribbed end-wall. Apparently, the ribs cannot completely stop the radial migration of the purge air flow, especially near the outer wall region. According to many previous study related to purge air cooling (Wright et al. [14], Knost and Thole [29], Nicklas [30], and Wright et al.[31]), additional film cooling is always needed to provide sufficient coverage to the end-wall. The ribbed end-wall concept should also be combined to conventional film cooling (or effusion cooling) to

overcome its limitation. However, results from the present study indicates that the needs from conventional end-wall cooling design should be greatly reduced.

For end-wall region with ribs, the heat load introduced by additional surface area needs to be taken into account. To fully assess the performance of ribbed structure, it may be more sensible to compare the total heat load rather than heat flux. A Net Heat Load Reduction (NHLR) can be expressed as,

$$NHLR = 1 - \frac{\int_{A_f} h_f (T_{ad} - T_w) dA_f}{\int_{A_0} h_0 (T_\infty - T_w) dA_0} = 1 - \frac{\int_{A_f} h_f \left({T_{ad}}/{T_w} - 1 \right) dA_f}{\int_{A_0} h_0 \left({T_\infty}/{T_w} - 1 \right) dA_0} \qquad (9)$$

where the temperature ratios T_∞/T_w, and T_{ad}/T_w can be replaced by typical values at engine conditions. The NHLR definition can be further simplified as follows:

$$NHLR = 1 - \frac{\int_{A_f} h_f (1 - \eta\varphi) dA_f}{\int_{A_0} h_0 dA_0} \qquad (10)$$

Distributions of NHLR along the duct passage is shown in Fig.24. As expected, the case with larger rib height (h/δ=0.25) does not show an overall improvement in heat load reduction due to some local poor coolant coverage. However, the case with reduced rib height (h/δ=0.15) gives consistent improvement for all the duct locations. An overall 11% improvement in NHLR is obtained.

In terms of practical design optimization strategy, the surface feature should be determined according to the incoming flow boundary layer characteristics, the purge air blowing ratio, blade loading, etc. Rib structure with variable heights along the flow passage should be able to achieve a better performance. Instead of protrusion, groove structure could also be implemented. It is exciting to know that such additional design

flexibility from the aerothermal perspective are being made feasible by the advances in Additive Manufacturing.

SUMMARY AND CONCLUSIONS

This paper presents the feasibility study of a novel end-wall flow control and thermal management concept. Purge air cooling performance with both smooth and ribbed end-wall was investigated in a simplified 90° turning duct through a combined experimental and numerical study. Transient thermal measurement was conducted in a low speed wind tunnel. Further analysis on the detailed flow structure was carried out by using a commercial CFD code.

The CFD analysis reveals that a ribbed end-wall can guide the purge air flow further to cover more end-wall surface. The secondary flow vortex can be reduced by the ribs blockage for cross-flow migration and the vortices generated in the rib grooves maintain the purge air attached to the end-wall. The film cooling effectiveness, heat transfer coefficient and NHFR obtained in transient thermal measurement consistently validate the numerical findings. With the addition of engineered surface structure, the film cooling effectiveness is significantly increased, the overall heat load can also be reduced even with the extra rib surface area.

It is suggested that the design of small-scale surface feature needs to be carefully optimized to ensure sufficient coolant coverage and avoid being burnt out in practical turbine application.

This novel engineered surface structure concept proposed in the present study provides a much improved design space and new research dimension in turbine end-wall cooling.

NOMENCLATURE

D	Duct width
d	Rib distance
H	Duct height
h	Rib height, Heat transfer coefficient
HTC	Heat transfer coefficient (W/(m2-K))
n	Rib number
q''	Heat flux (W/m2)
r_i	Duct inner radius
r_o	Duct outer radius
R^2	Coefficient of determination
R/D	Radial-wise measurement location normalized by duct width
SSE	Sum of square error
SST	Total corrected sum of squares

T	Local temperature
T_{ad}	Adiabatic wall temperature
T_b	Blade metal temperature
T_p	Purge air temperature
T_r	Recovery temperature
T_w	End-wall temperature
T_∞	Mainstream temperature
V_∞	Inlet velocity
w	Rib width
Y/P	Pitch-wise measurement location normalized by pitch
$y+$	Non-dimensional wall distance: $y^+ \equiv u_\tau y / \nu$
Z/H	Span-wise measurement location normalized by duct height
NHFR	Net heat flux reduction
NHLR	Net heat load reduction $NHLR = 1 - \dfrac{\int_{A_f} h_f (1-\eta\varphi) dA_f}{\int_{A_0} h_0 dA_0}$
β	Relative angle between streamwise direction and x-axis
θ	Non-dimensional fluid temperature
δ	Boundary layer thickness
φ	Non-dimensional metal temperature

η Film cooling effectiveness

Ω Vorticity

REFERENCES

[1] Han, J.C., 2004, "Recent studies in turbine blade cooling," International Journal of Rotating Machinery, 10(6), pp.443-457.

[2] Bunker, R.S., Metzger, D.E. and Wittig, S., 1992, "Local Heat Transfer in Turbine Disk Cavities: Part I—Rotor and Stator Cooling with Hub Injection of Coolant," Journal of Turbomachinery, 114, p.211.

[3] Bunker, R.S., Metzger, D.E. and Wittig, S., 1992, "Local Heat Transfer in Turbine Disk Cavities: Part II—Rotor Cooling with Radial Location Injection of Coolant," Journal of Turbomachinery, 114(1), pp.221-228.

[4] Wilson, M., Arnold, P.D., Lewis, T.W., Mirzaee, I., Rees, D.A.S. and Owen, J.M., 1997, "Instability of flow and heat transfer in a rotating cavity with a stationary outer casing," Eurotherm 55 (Heat Transfer in a Single Phase Flow).

[5] McLean, C., Camci, G., and Glezer, B., 2001, "Mainstream aerodynamic effects due to wheelspace coolant injection in a high-pressure turbine stage," Journal of Turbomachinery, 123(4), pp.687-703.

[6] McLean, C., Camci, C., and Glezer, B., 2001, "Mainstream Aerodynamic Effects Due to Wheelspace Coolant Injection in a High-Pressure Turbine Stage: Part II—Aerodynamic Measurements in the Rotational Frame," Journal of Turbomachinery, 123(4), pp.697-703.

[7] Girgis, S., Vlasic, E., Lavole, J.P. and Moustapha, S.H., 2002, "The effect of secondary air injection on the performance of a transonic turbine stage," ASME Paper No. GT2002-30340.

[8] Reid, K., Denton, J., Pullan, G., Curtis, E. and Longley, J., 2006, "The effect of stator-rotor hub sealing flow on the mainstream aerodynamics of a turbine," ASME Paper No. GT2006-90838.

[9] Roy, R.P., Squires, K.D., Gerendas, M., Song, S., Howe, W.J. and Ansari, A., 2000, "Flow and Heat Transfer at the Hub Endwall of Inlet Vane Passages—Experiments and Simulations," ASME Paper No. 2000-GT-0198.

[10] Burd, S.W., Satterness, C.J. and Simon, T.W., 2000, "Effects of Slot Bleed Injection Over a Contoured End Wall on Nozzle Guide Vane Cooling Performance: Part II—Thermal Measurements," ASME Paper No. 2000-GT-0200.

[11] Oke, R., Simon, T., Shih, T., Zhu, B., Lin, Y.L., and Chyu, M., 2001, "Measurements over a Film-Cooled Contoured Endwall with Various Coolant Injection Rates," ASME Paper No. 2001-GT-0140.

[12] Dénos, R. and Paniagua, G., 2002, "Influence of the Hub Endwall Cavity Flow on the Time-Averaged and Time-Resolved Aero-Thermodynamics of Axial HP Turbine Stage," ASME Paper No. GT2002-30185.

[13] Wright, L.M., Gao, Z., Yang, H. and Han, J.C., 2008, "Film Cooling Effectiveness Distribution on a Gas Turbine Blade Platform with Inclined Slot Leakage and Discrete Film Hole Flows," Journal of Heat Transfer, 130(7), p.071702.

[14] Wright, L.M., Blake, S.A., and Han, J.C., 2006, "Film Cooling Effectiveness Distributions on a Turbine Blade Cascade Platform with Stator-Rotor Purge and Discrete Film Hole Flows," In ASME 2006 International Mechanical Engineering Congress and Exposition (pp. 489-498). American Society of Mechanical Engineers.

[15] Popovic, I. and Hodson, H.P., 2010, "Aerothermal Impact of the Interaction Between Hub Leakage and Mainstream Flows in Highly-Loaded HP Turbine Blades," ASME Paper No. GT2010-22311.

[16] Miao, X., Zhang, Q., Atkin, C. and Sun, Z., 2016, "End-Wall Secondary Flow Control Using Engineered Residual Surface Structure," ASME Paper No. GT2016-57347

[17] Miao, X., Zhang, Q., Wang, L., Jiang, H., & Qi, H, 2015, "Application of riblets on turbine blade endwall secondary flow control," Journal of Propulsion and Power, 31(6), 1578-1585.

[18] Camci, C. and Rizzo, D.H., 2002, "Secondary flow and forced convection heat transfer near endwall boundary layer fences in a 90 turning duct," International Journal of Heat and Mass Transfer, 45(4), pp.831-843.

[19] Schulz, A., 2000, "Infrared Thermography as Applied to Film Cooling of Gas Turbine Components." Measurement Science and Technology, vol. 11, no. 7, pp. 948.

[20] O'Dowd, D.O., Zhang, Q., He, L., Ligrani, P.M. and Friedrichs, S., 2011, "Comparison of heat transfer measurement techniques on a transonic turbine blade tip," Journal of Turbomachinery, 133(2), p.021028.

[21] Zhang, Q., He, L., Wheeler, A.P.S., Ligrani, P.M. and Cheong, B.C.Y., 2011, "Overtip shock wave structure and its impact on turbine blade tip heat transfer," Journal of Turbomachinery, 133(4), p.041001.

[22] Zhang, Q., O'Dowd, D.O., He, L., Oldfield, M.L.G. and Ligrani, P.M., 2011, "Transonic Turbine Blade Tip Aerothermal Performance with Different Tip Gaps—Part I: Tip Heat Transfer," Journal of Turbomachinery, 133(4), p.041027.

[23] Zhang, Q., He, L., Cheong, B.C.Y. and Tibbott, I., 2013, "Aerothermal performance of a cooled winglet at engine representative Mach and Reynolds numbers," Journal of Turbomachinery, 135(1), p.011041.

[24] Oldfield, M.L., 2008. Impulse response processing of transient heat transfer gauge signals. Journal of Turbomachinery, 130(2), p.021023.

[25] Ma, H., Zhang, Q., He, L., Wang, Z. and Wang, L., 2017, "Cooling Injection Effect on a Transonic Squealer Tip—Part I: Experimental Heat Transfer Results and CFD Validation," Journal of Engineering for Gas Turbines and Power, 139(5), p.052506.

[26] Moffat, R. J., 1988, "Describing the Uncertainties in Experimental Results," Experimental Thermal and Fluid Science, vol. 1, pp. 3–17.

[27] Devore, J.L., 2011, "Probability and Statistics for Engineering and the Sciences," Cengage learning.

[28] Sen, B., Schmidt, D.L., and Bogard, D.G., 1996, "Film Cooling with Compound Angle Holes: Heat Transfer", ASME J. of Turbomachinery, Vol. 118.

[29] Knost, D. and Thole, K., 2005, "Adiabatic effectiveness measurements of endwall film-cooling for a first-stage vane," Journal of turbomachinery, 127(2), pp.297-305.

[30] Nicklas, M., 2001, "Film-cooled turbine endwall in a transonic flow field: Part ii—heat transfer and film-cooling effectiveness," Journal of Turbomachinery, 123(4), pp.720-729.

[31] Wright, L.M., Blake, S. and Han, J.C., 2007, "Effectiveness Distributions on Turbine Blade Cascade Platforms Through Simulated Stator-Rotor Seals," Journal of thermophysics and heat transfer, 21(4), pp.754-762.

Figure Captions List

Table Caption List

Table 1   Geometry of ribs array on the end-wall.

Table 2   Measurement uncertainties

Figure 1. A schematic of the experiment facility employed in the present study.
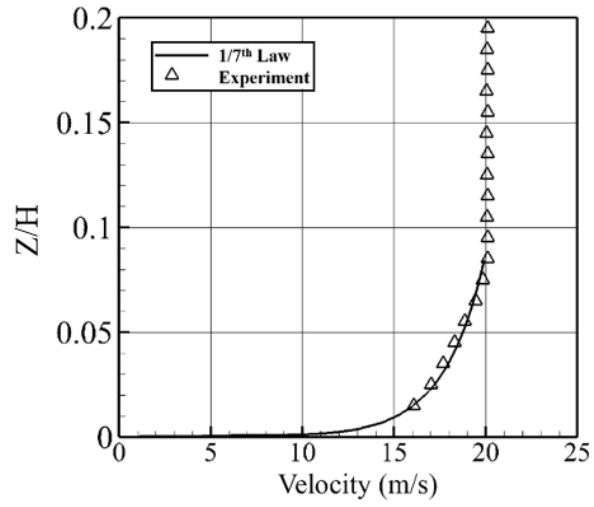
Figure 2. Inlet end-wall turbulent boundary layer velocity profile.
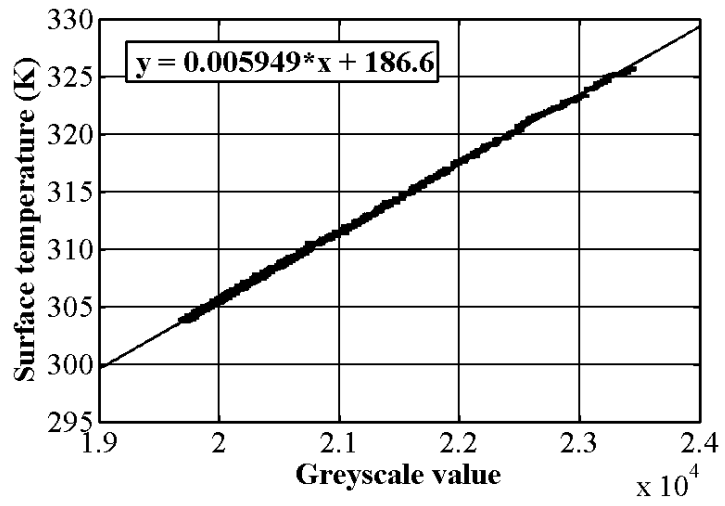
Figure 3. IR camera in-situ calibration curve.
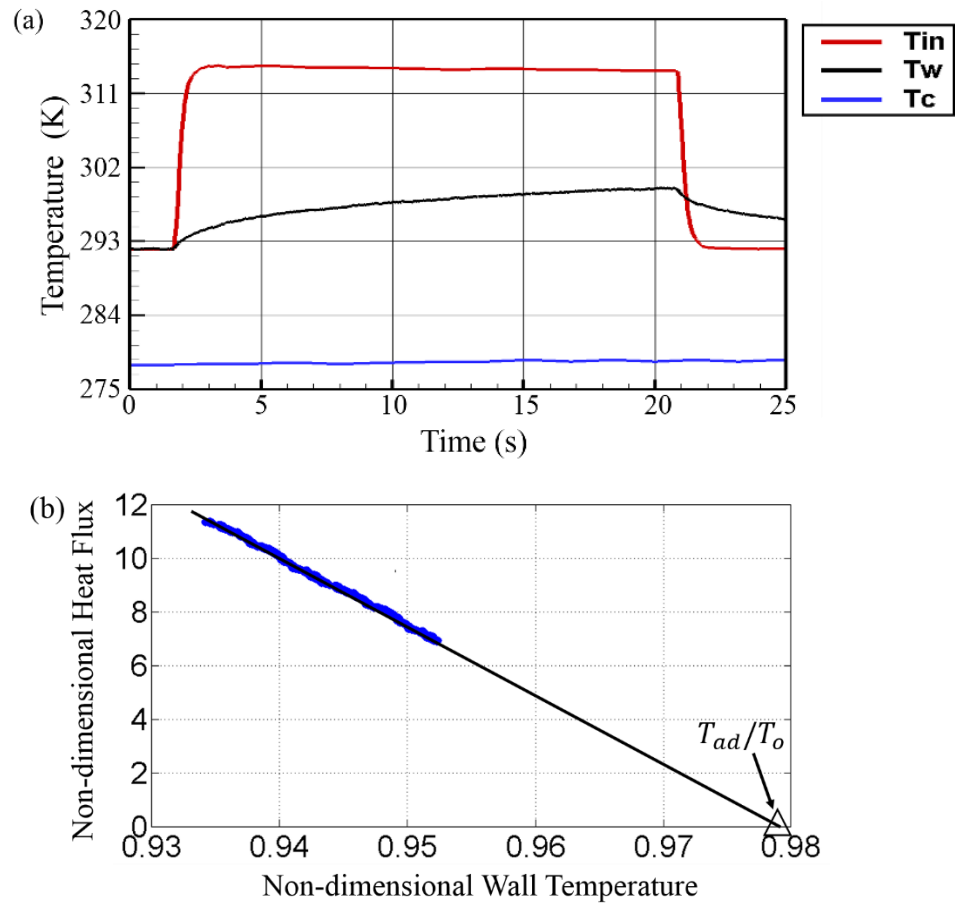
Figure 4. (a) Time histories of the cold purge air, end-wall and inlet temperatures, and (b) variations of wall heat flux and surface temperature for one selected location, during one typical transient measurement.
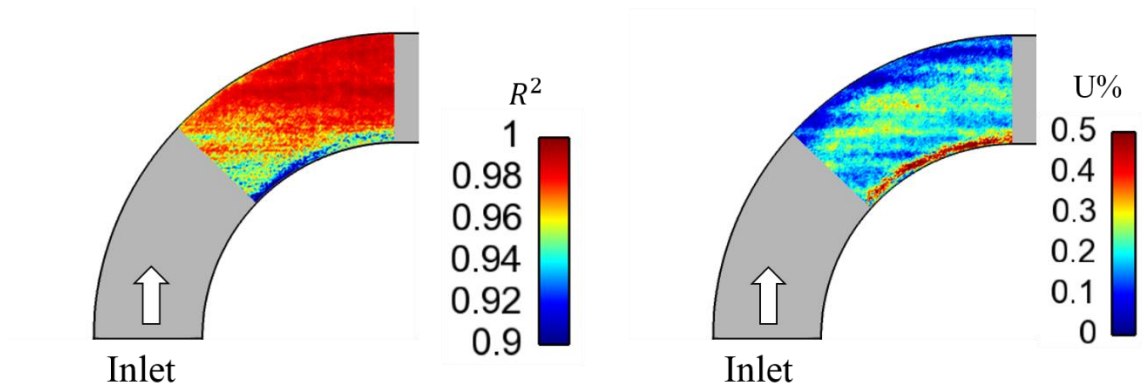
Figure 5. (a) R^2 distribution for linear regression, and (b) Relative uncertainty ($\%U$) in T_{ad} distribution.
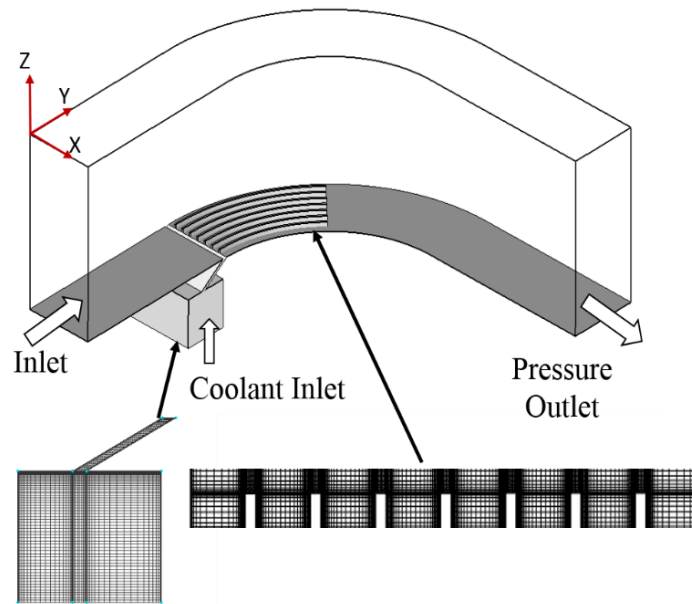
Figure 6. The computational domain and grids employed in the present study.
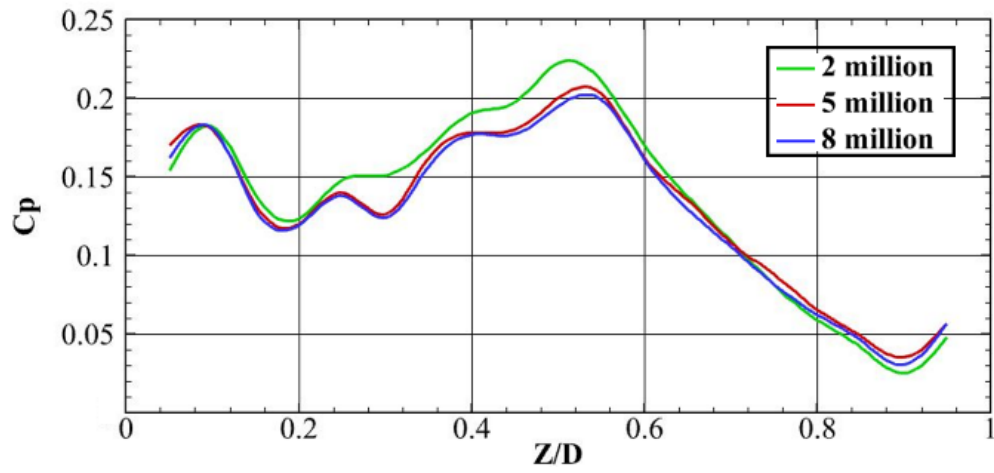
Figure 7. Spanwise-averaged total pressure loss coefficient C_p

Experimental
study
(Camci and Rizzo)

(a)

(b)

CFD

(c)

(d)

C_p

1.2

0.6

0

No fence
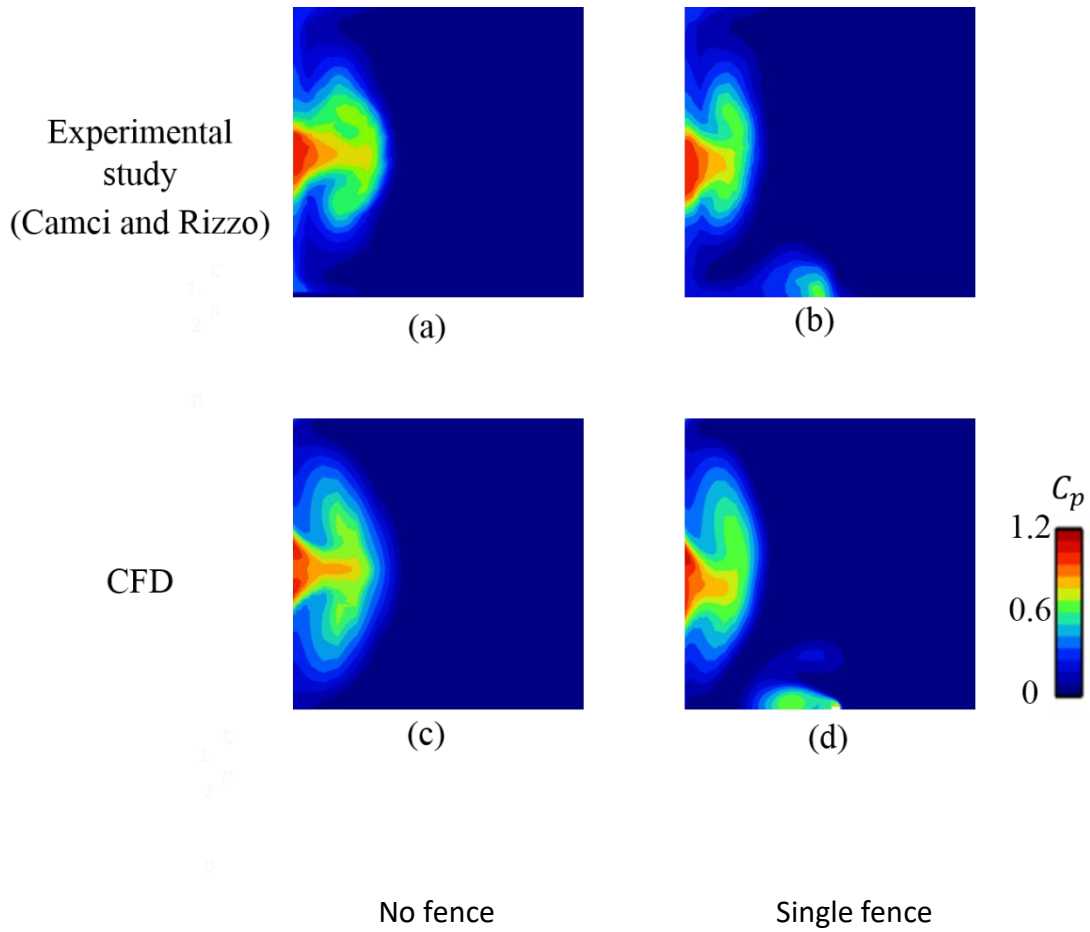
Single fence

Figure 8. Total pressure loss coefficient C_p distributions for cases with and without single fence obtained at 90-degree plane of the duct.
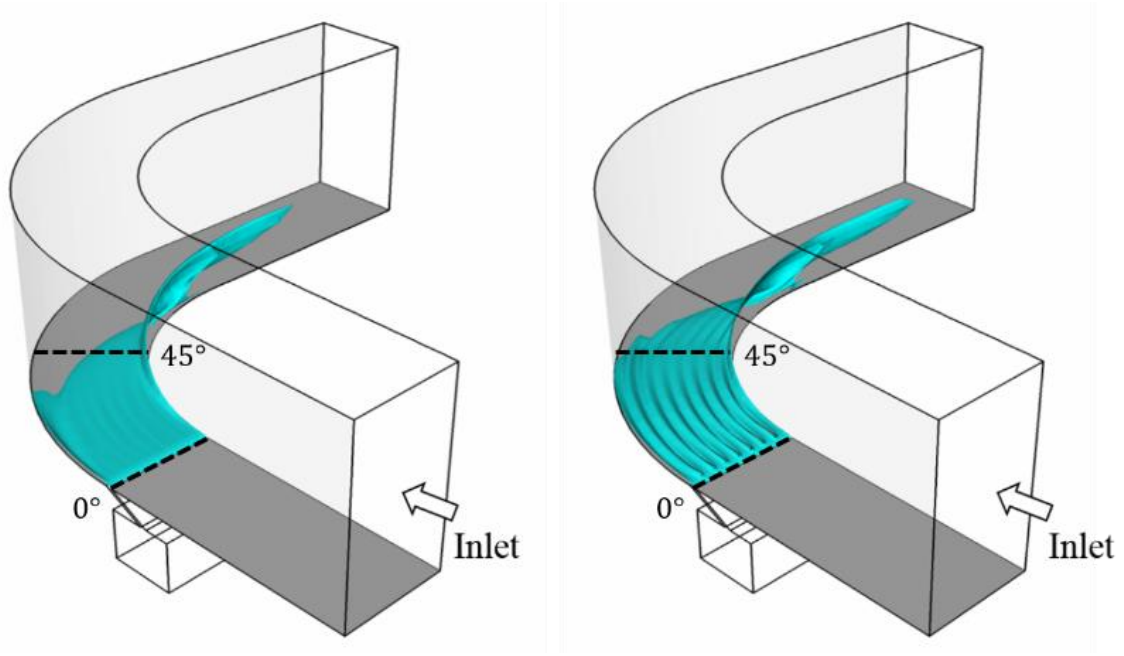
(a) Smooth surface   (b) Ribbed surface

Figure 9. An iso-temperature surface with $\theta = 0.6$.
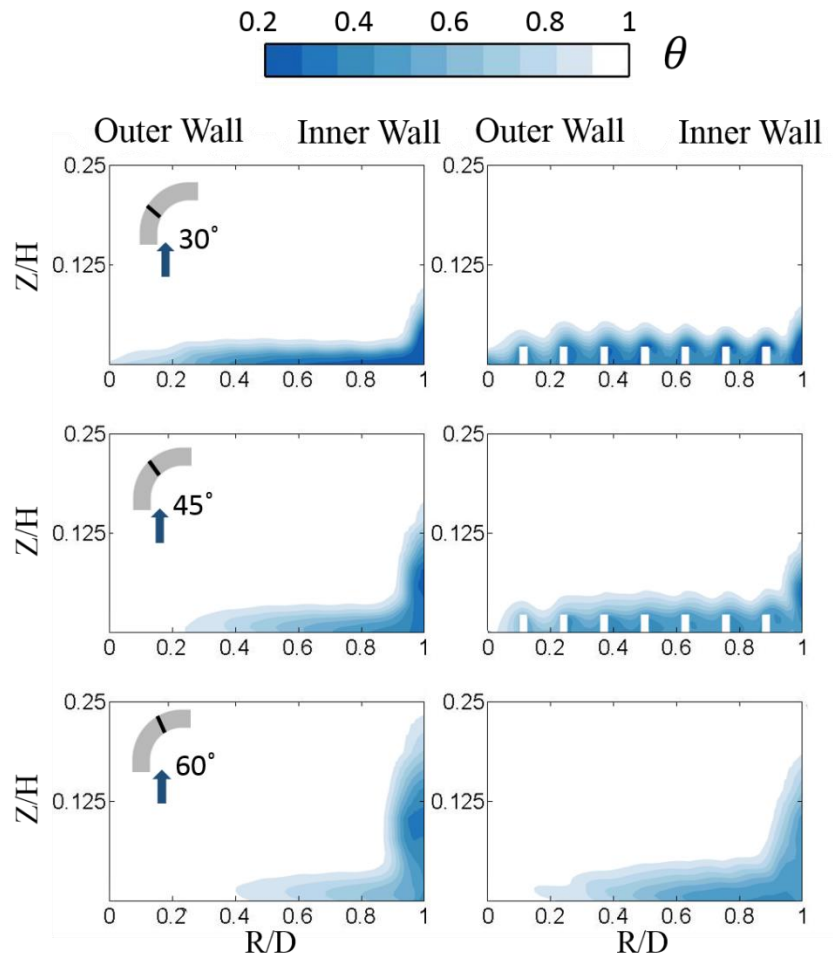
(a) Smooth surface   (b) Ribbed surface

Figure 10. Non-dimensional temperature θ distribution at three angular cross sections.
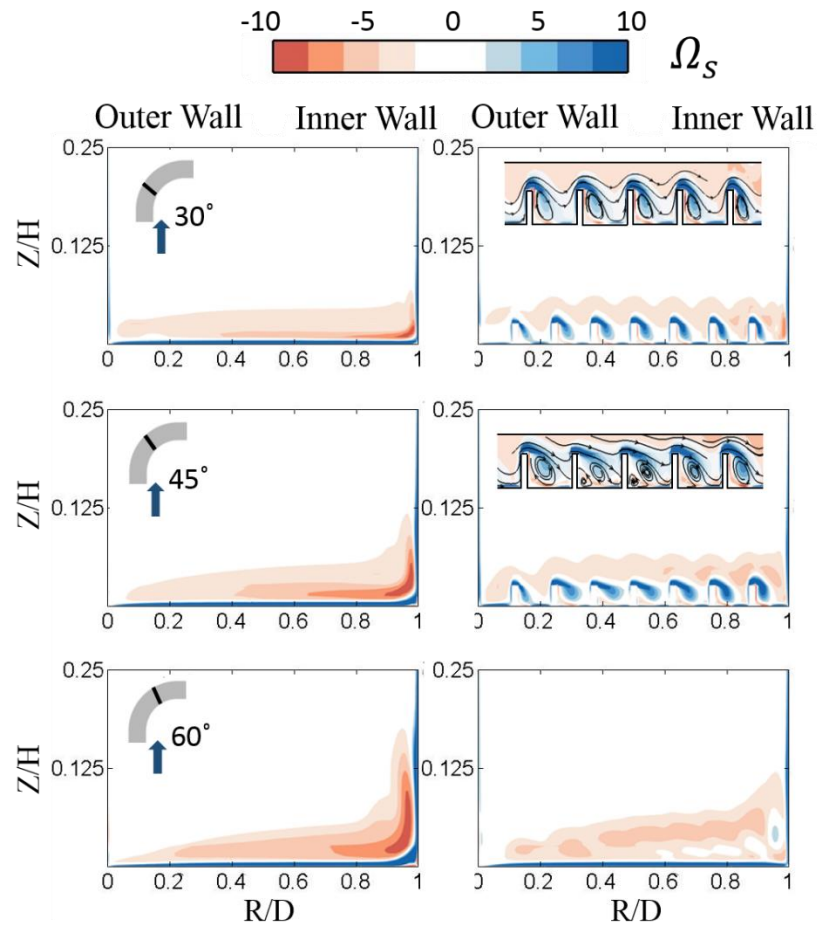
(a) Smooth surface   (b) Ribs surface

Figure 11. Streamwise vorticity distributions at three angular cross sections.

(a) Smooth surface   (b) Ribbed surface
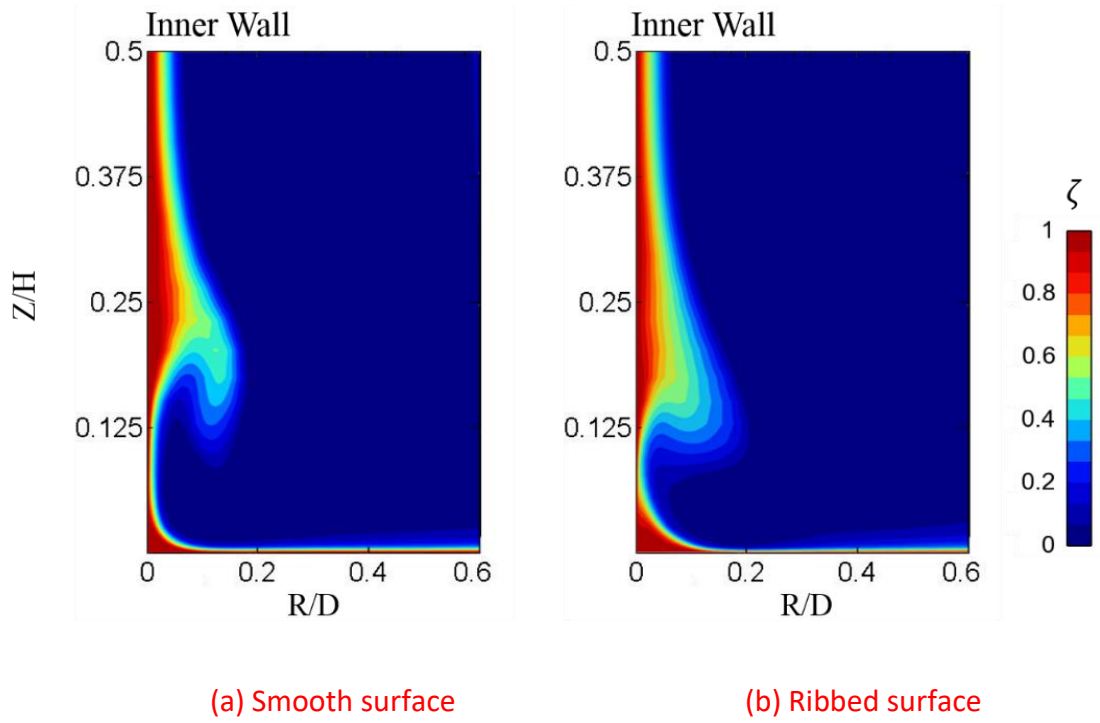
Figure 12. Distributions of Aerodynamic loss coefficient at the exit plane.
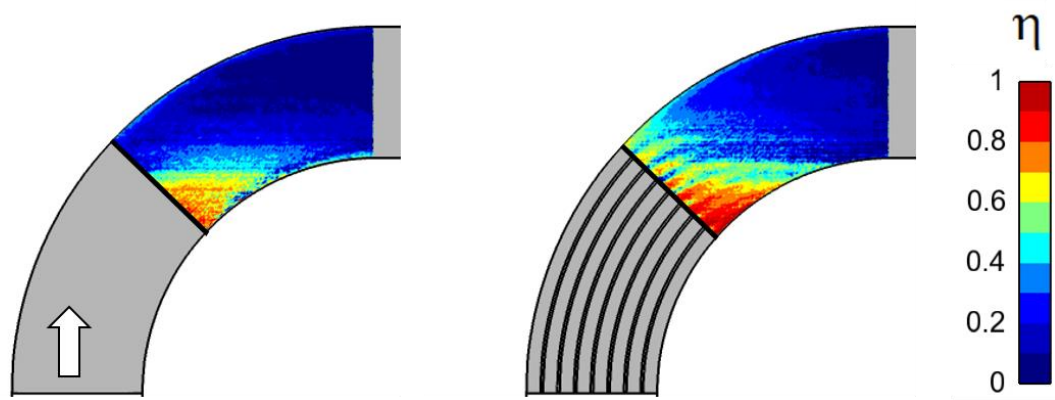
(a) Smooth surface   (b) Ribbed surface

Figure 13. Film cooling effectiveness (experimental data).
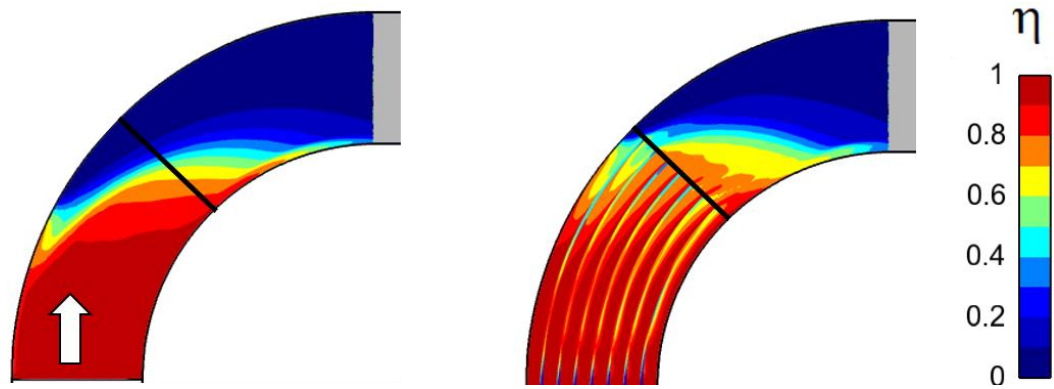
(a) Smooth surface   (b) Ribbed surface

Figure 14. Film cooling effectiveness (CFD results).
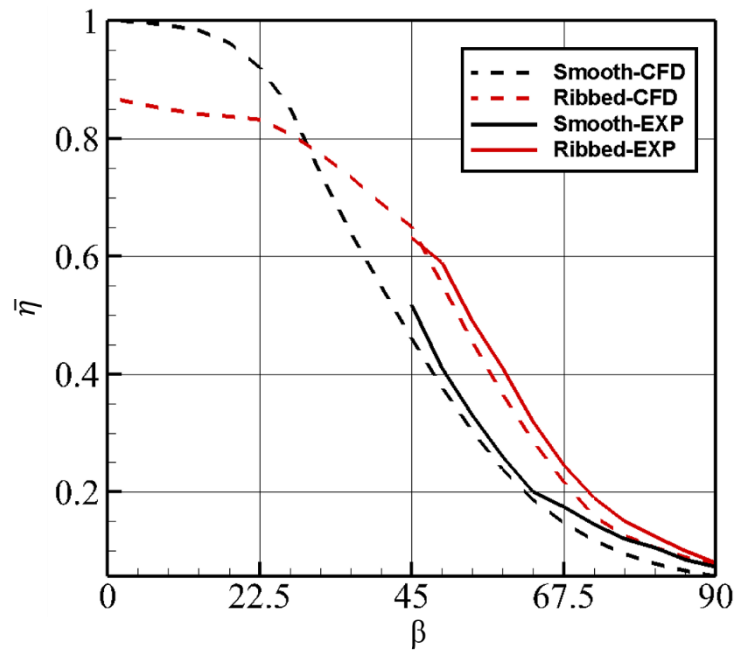
Figure 15. Laterally film cooling effectiveness $\bar{\eta}$ along the duct passage for both experimental and CFD results.
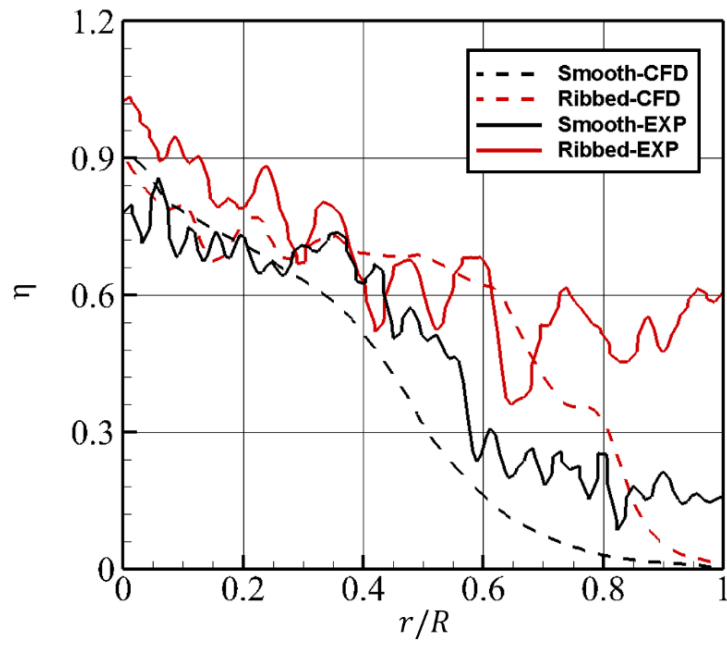
Figure 16. Film cooling effectiveness variation along the radius direction.
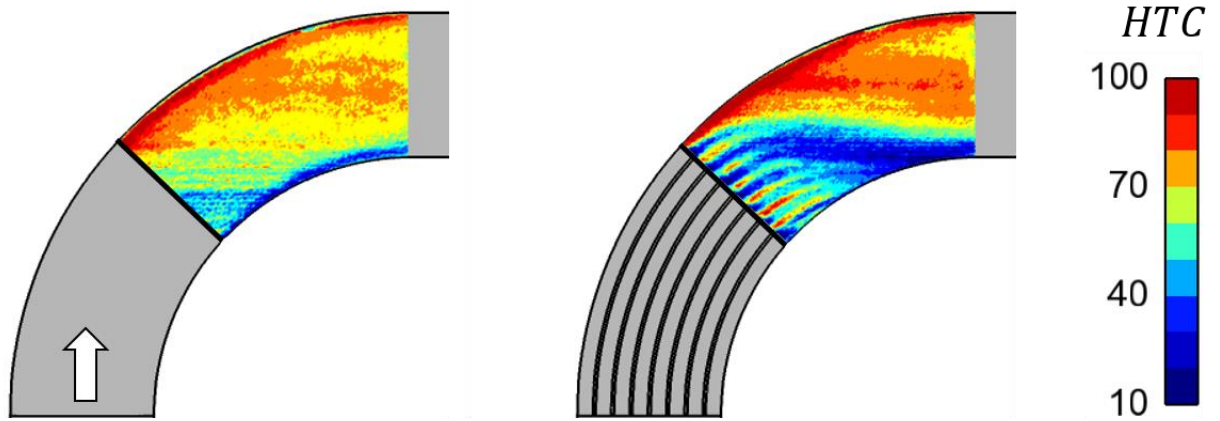
(a) Smooth surface   (b) Ribbed surface

Figure 17. Distribution of heat transfer coefficient (experimental data).
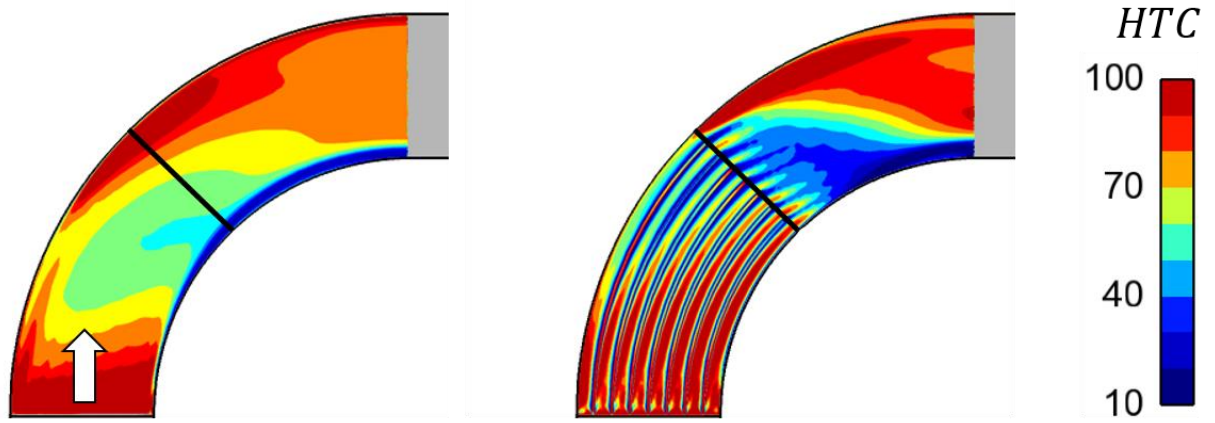
(a) Smooth surface　　　　　　　　　(b) Ribbed surface

Figure 18. Distributions of heat transfer coefficient (CFD).
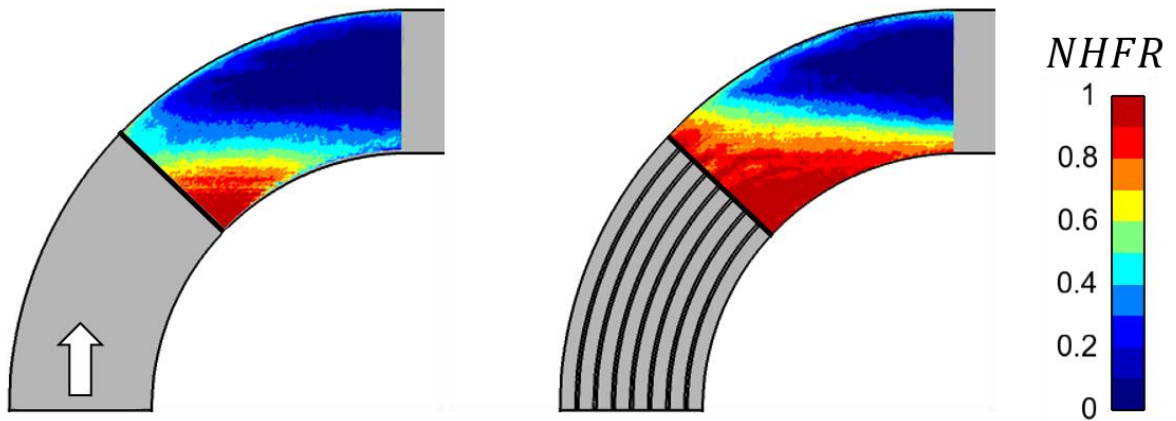
(a) Smooth surface   (b) Ribbed surface

Figure 19. Distributions of NHFR (experimental data).
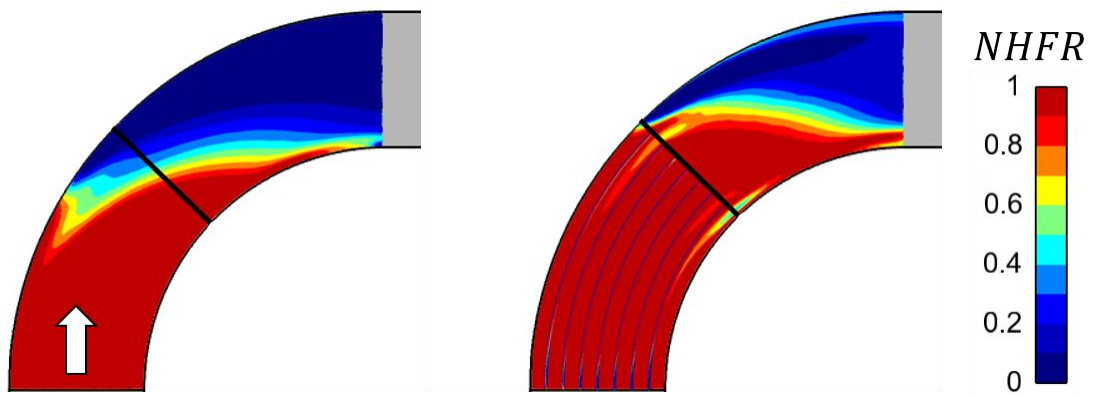
(a) Smooth surface   (b) Ribbed surface

Figure 20. Distributions of NHFR (CFD results).

(a) h/δ=0.25   (b) h/δ=0.15
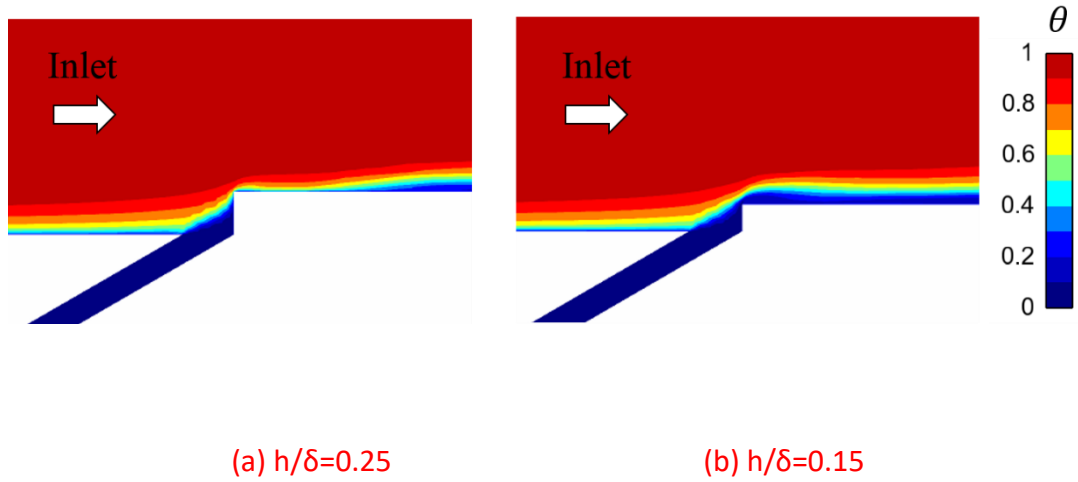
Figure 21. Non-dimensional temperature θ distribution near the purge air entry region for ribbed surface.
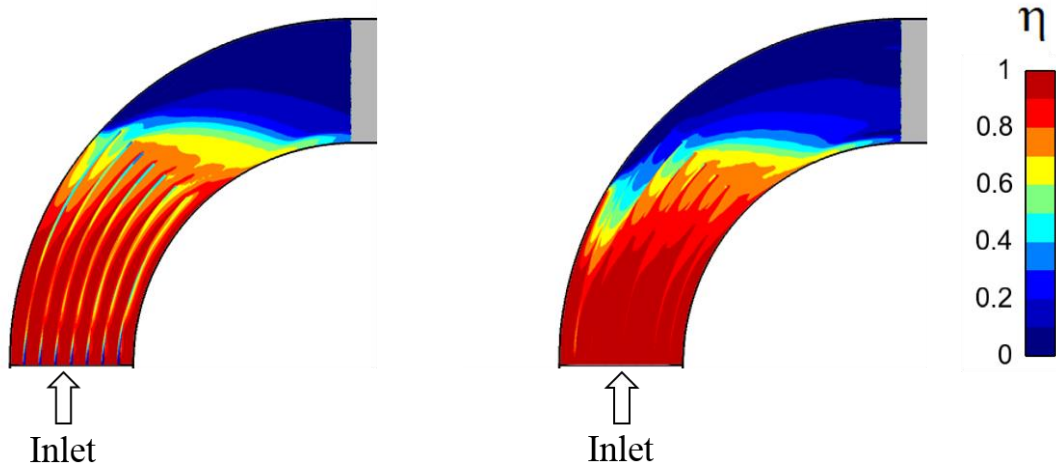
(a) h/δ=0.25   (b) h/δ=0.15

Figure 22. Distributions of film cooling effectiveness.

(a) Smooth surface　　　　(b) Ribbed surface h/δ=0.25　　　(c) Ribbed surface h/δ=0.15
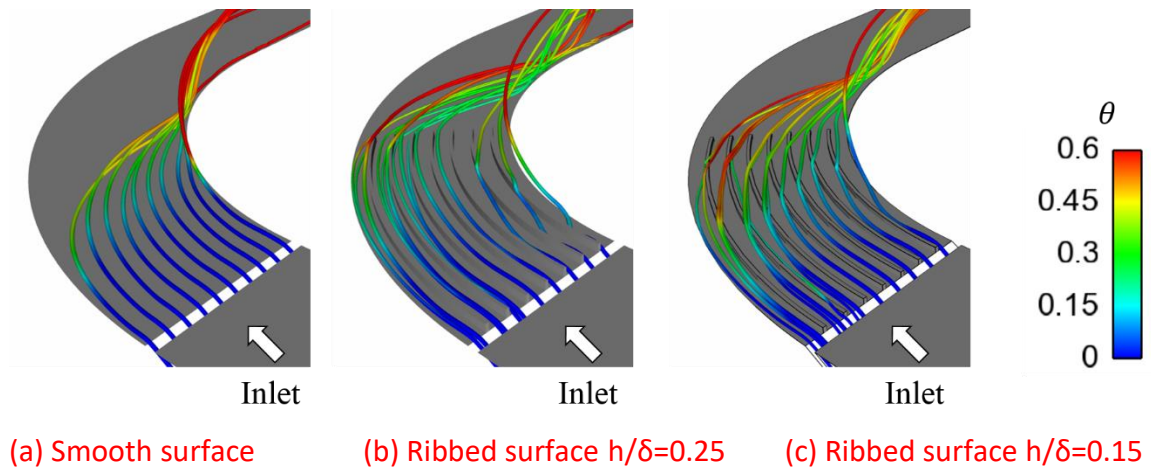
Figure 23. Cooling fluid streamlines near the end-wall ribs.
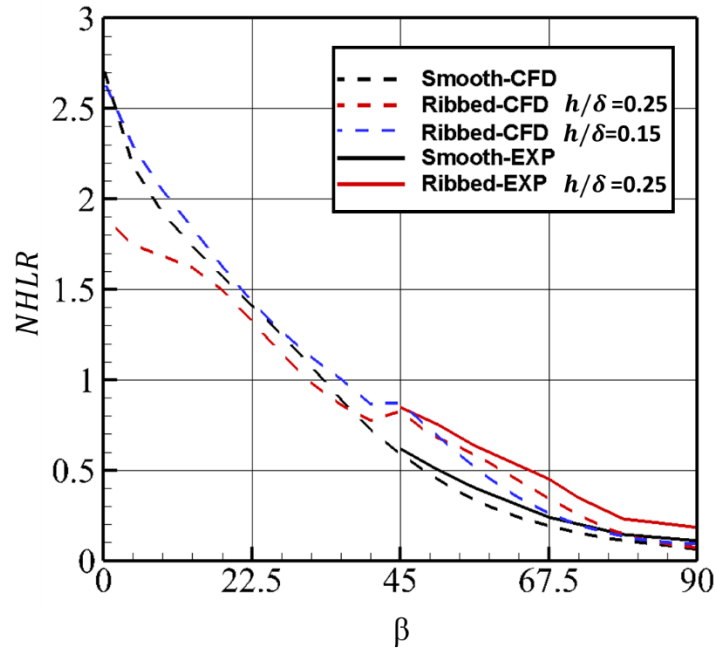
Figure 24. Distributions of Net Heat Load Reduction along the duct passage.

Table 1. Geometry of ribs array on the end-wall.
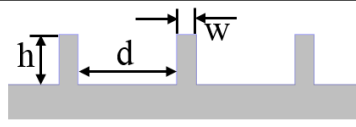
w/h	0.4
d/h	2.15
δ/h	4

Table 2. Measurement uncertainties

Measurement	Relative uncertainty 95% confidence
Material property	5% (564 ± 28 $\sqrt{s}$/m^{2}K)
Measured wall temperature	1K
h	8.7%
T_{ad}	0.26%